CHALMERS
UNIVERSITY OF TECHNOLOGY

# Modeling of coupled dual-scale flow–deformation processes in composites manufacturing

Citation for the original published paper (version of record):
Rouhi, M., Wysocki, M., Larsson, R. (2013). Modeling of coupled dual-scale flow–deformation processes in composites manufacturing. Composites Part A: Applied Science and Manufacturing, 46(1): 108-116. http://dx.doi.org/10.1016/j.compositesa.2012.11.002

Composites: Part A 46 (2013) 108–116

Contents lists available at SciVerse ScienceDirect

Composites: Part A

journal homepage: www.elsevier.com/locate/compositesa

# Modeling of coupled dual-scale flow–deformation processes in composites manufacturing

Mohammad S. Rouhi [a,b], Maciej Wysocki [b,a,*], Ragnar Larsson [a]

[a] Division of Material and Computational Mechanics, Department of Applied Mechanics, Chalmers University of Technology, SE-412 96 Göteborg, Sweden
[b] Swerea Sicomp, P.O. Box 104, SE-431 22 Mölndal, Sweden

ARTICLE INFO

Article history:
Received 19 September 2012
Received in revised form 1 November 2012
Accepted 14 November 2012
Available online 29 November 2012

Keywords:
C. Finite Element Analysis (FEA)
E. Consolidation
E. Forming
Poromechanics

ABSTRACT

The present contribution is a part of the work towards a framework for holistic modeling of composites manufacturing. Here we focus our attention onto the particular problem of coupled dual-scale deformation–flow process such as the one arising in RTM, Vacuum Assisted Resin Infusion (VARI) and Vacuum Bag Only (VBO) prepregs. The formulation considers coupling effects between macro-scale preform processes and meso-scale ply processes as well as coupling effects between the solid and fluid phases. The framework comprises a nonlinear compressible fiber network saturated with incompressible fluid phase. Internal variables are introduced in terms of solid compressibility to describe the irreversible mesoscopic infiltration and reversible preform compaction processes. As a main result a coupled displacement–pressure, geometrically nonlinear, finite element simulation tool is developed. The paper is concluded with a numerical example, where a relaxation–compression test of a planar fluid filled VBO preform at globally un-drained and partly drained conditions is considered.

## 1. Introduction

Traditional processing of high quality composite materials requires autoclave consolidation and curing at elevated pressure and temperature. Composite parts cured inside an autoclave have excellent quality; however, this quality comes with a high price tag. Recent developments in prepreg technology have led to the development of an Out-Of-Autoclave (OOA) prepreg that can be cured with only vacuum pressure and lower temperatures [1]. Vacuum Bag Only (VBO) prepregs are a member of the family of OOA techniques for composite manufacturing in which composite laminates are produced from prepregs by vacuum-bag consolidation followed by curing in an oven [2]. The advantages of VBO over autoclave processing are lower capital investment, elimination of the need for costly nitrogen gas, greater energy efficiency and reduction of size constraints (larger parts) [3].

As the resin flow through fiber bed is often the single most important processing step in composites manufacturing, it has been investigated by many researchers [4]. Many efforts in modeling flow and infiltration have been carried out by assuming that the different scales are treated in an uncoupled fashion and the fiber bed often assumed stationary, cf. e.g. [5–9]. Moreover, it is well established [10] that a true processing operation will result in dual-scale flow, resulting in a number of successful attempts to predict the study of the dual scale flow [11–19]. Unfortunately, only a few of these have focused on the fiber bed saturation coupled to the motion of the fiber bed and resin flow [10,20–24]. In this context, we note that both VARI as well as consolidation of VBO prepregs is due to external pressure at elevated temperature resulting in coupled resin flow and fiber bed deformations. In addition, during this process two coupled flows may be present: inter- and intra-ply (bundle) flows [25,26]. The inter-ply flow is the flow through the wide channels between the plies, whereas the flow between the fibers inside the plies is the intra-ply flow. Presently there are only few publications that can handle resin flow and fiber bed deformations and also limited number of publications onto the modeling of two-scale processes. Unfortunately, to the authors' knowledge, there are no published models capable of simultaneous modeling of the coupled deformations–flow at two different scales in the finite strain regime.

Larsson et al. [27] proposed a method to predict the consolidation involving coupled micro- and macro-resin flow based on a two-phase porous media theory formulation. The considered processes involve deformation of a fiber bed network at completely un-drained conditions, wetting by penetration of resin into fiber plies, and resin flow (affine with the preform velocity) through the fiber bed network. In the present work we extend the developments in [24,27] to allow for more general (anisotropic) resin flow at drained conditions. Similarly to [27] the emphasis is placed on

---

* Corresponding author at: Swerea SICOMP, P.O. Box 104, SE-431 22 Mölndal, Sweden. Tel.: +46 (0)31 706 6341.
E-mail address: maciej.wysocki@swerea.se (M. Wysocki).

1359-835X
http://dx.doi.org/10.1016/j.compositesa.2012.11.002

the modeling of solid compressibility, due to micro-level wetting and volumetric change of the fiber network, and the modeling of macroscopic resin flow in the deforming preform.

The paper is outlined as follows: (1) the involved micro-constituents are identified and expressed using the relevant variables at the micro-level; (2) the governing equations of a biphasic compressible theory of porous media are reiterated; (3) the associated entropy inequality is considered in terms of three independent dissipative mechanisms: (i) deformation of the solid phase, (ii) intrinsic compressibility in the solid phase and (iii) Darcian interaction between the phases; (4) the dissipations in the solid phase are derived at a micro-mechanical level, and a model for the irreversible wetting process is established in terms of a logarithmic intrinsic compaction strain in the solid phase. In this development, an exponential packing law, cf. [28], is proposed to link the fluid pressure to the intrinsic compression of the solid phase. Moreover, to describe the wetting process, a linear visco-elastic evolution law is proposed for the evolution of wetting, whereby positive dissipation can be ensured; (5) the boundary value problem is formulated with respect to nonlinear kinematics and drained conditions; (6) the paper is concluded by a numerical example of the volumetric deformation–pressure response of a fluid saturated fiber composite specimen. To simplify the analysis in the example the preform is considered isotropic in terms of a linear shear stiffness and power law type of response for the volumetric deformations.

## 2. Micro-constituents and solid phase compaction

To begin with, let us establish the link between micro- and macro constituents in terms of a representative mixture (having volume $V$) consisting of three different micro-scale constituents, as depicted in Fig. 1. The micro-constituents of the mixture are the following:

- Incompressible solid particles, $p$ with the volume fraction $\phi^p = V^p/V$, representing the fibers.
- Incompressible liquid constituent, $l$ with the volume fraction $\phi^l = V^l/V$, representing the resin.
- Voids, $v$ with volume fraction $\phi^v = V^v/V$, embedded in the fiber plies.

In order to ensure that each representative control volume of the solid is occupied with the fluid and solid/void mixture where we have the saturation constraint

$$\phi^p + \phi^l + \phi^v = 1. \tag{1}$$

We also relate to the two-phase porous media theory, where the micro-constituents are considered homogenized. In particular, the macroscopic volume fractions for the solid and the fluid phases, $n^s$ and $n^f$, are defined as

$$n^s = \frac{V^s}{V} = \frac{V^p + V^v}{V}, \quad n^f = \frac{V^f}{V} = \frac{V^l}{V}. \tag{2}$$

In view of Eq. (1), we also have the saturation constraint

$$n^s + n^f = 1 \quad \text{with} \quad n^s = \phi^p + \phi^v \quad \& \quad n^f = \phi^l. \tag{3}$$

As to the modeling of fluid infiltration of fiber plies, the partially saturated fibers (named particles) are subdivided into a wet portion (already penetrated by resin fluid) and a dry portion $\phi^{pd}$, as shown in Fig. 2. Hence, the fiber content $\phi$ in the dry region of the fiber bed is obtained as

$$\phi = \frac{\phi^{pd}}{\phi^{pd} + \phi^v}, \tag{4}$$

where the particle portion is defined by wet particles and dry particles, in terms of a saturation ratio $\xi$ defining the degree of wet out within a representative fiber ply, defined by

$$\xi = \frac{\phi^p - \phi^{pd}}{\phi^p}, \tag{5}$$

whereby the fiber content $\phi$ in the dry region can be resolved as

$$\phi = \frac{\phi^p - \xi\phi^p}{n^s + \xi\phi^p}. \tag{6}$$

Observing that in the typical vacuum assisted process the influence of pore gas contribution in the mass balance can be neglected, leads to the relation $n^s\rho^s = \phi^p\rho^p$ whereby Eq. (6) becomes

$$\phi = (1 - \xi)\left(\frac{\rho^p}{\rho^s} - \xi\right)^{-1}. \tag{7}$$

where $\rho$'s are the densities. It may be noted that we have the initial condition at $\xi \to 0$ leading to $\phi_0 = \rho_0^s/\rho^p$. We thereby also have $\rho^s \to \rho_0^s/\phi_0$, which in combination with Eq. (7) gives the compaction of the solid phase as a function of irreversible wetting factor $\xi$ and the reversible packing volume fraction $\phi$ in terms of

$$\frac{\rho_0^s}{\rho^s} = \frac{\phi_0}{\phi}\frac{1 - \xi(1 - \phi)}{1 - \xi(1 - \phi_0)}(1 - \xi(1 - \phi)). \tag{8}$$

Taking the logarithm of Eq. (8) yields the additive decomposition of the total compaction strain $\varepsilon$ as

$$\begin{aligned}\varepsilon &= \log\left[\frac{\rho_0^s}{\rho^s}\right] = \log\left[\frac{\phi_0}{\phi}\frac{1 - \xi(1 - \phi)}{1 - \xi(1 - \phi_0)}\right] + \log[1 - \xi(1 - \phi_0)] \\ &= \varepsilon^e + \varepsilon^p,\end{aligned} \tag{9}$$

where the reversible compaction strain $\varepsilon^e$ (related to the packing $\phi$ and the saturation degree $\xi$) and the irreversible wetting compaction $\varepsilon^p$ (related only to the saturation degree $\xi$) are defined.

## 3. A homogenized theory of porous media

Assuming that the void motion is affine with the particle motion, the micro problem of three actual constituents in the mixture

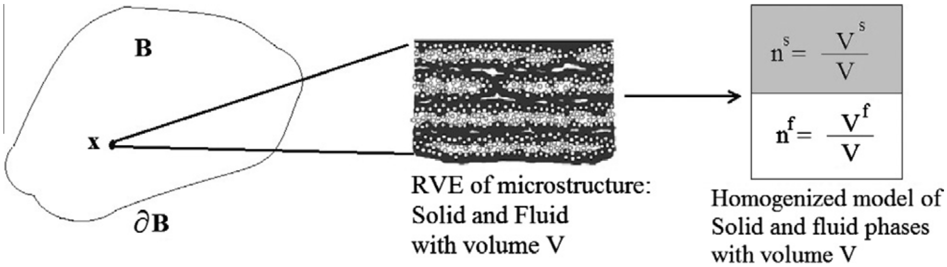

**Fig. 1.** Homogenized theory of porous media.

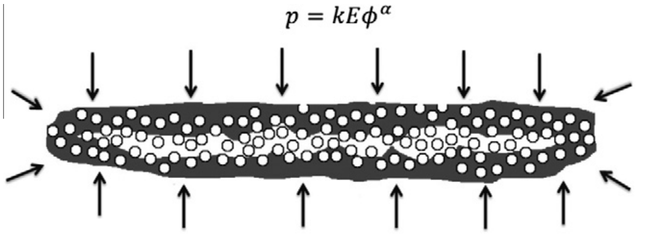

**Fig. 2.** Hyperelastic packing of fiber content $\phi$ in dry region induced by fluid pressure of representative fiber ply in the fiber bed at a fixed value of the micro-infiltration $\xi$.

may be reduced to a two-phase continuum problem. We thereby focus our attention to the formulation of a binary continuum model, consisting of a compressible solid phase, *s*, and an incompressible fluid phase, *f*. Following the developments in [29] we model the problem using the following governing equations.

### 3.1. Mass and momentum balance

Due to conservation of the mass of the two considered phases we have the following relationships

$$\dot{M}^s = 0, \quad \dot{M}^f + J\,\nabla\cdot(\rho^f \boldsymbol{v}^d) = 0, \tag{10}$$

where $M^s$ and $M^f$ are the solid and fluid content respectively, $J$ is the Jacobean of the deformation gradient, $\rho^f$ is the fluid density and $\boldsymbol{v}^d$ is the Darcian velocity defined from the relative velocity between phases $\boldsymbol{v}^r = \boldsymbol{v}^s - \boldsymbol{v}^f$ as $\boldsymbol{v}^d = n^f\boldsymbol{v}^r$, where $\boldsymbol{v}^s$ is the solid phase velocity and $\boldsymbol{v}^f$ is the fluid phase velocity. In particular, the stationarity of $M^s$ leads to $n^s\rho^s J = n_0^s\rho_0^s$, whereby the solid volume fraction is governed by the relation

$$n^s = \frac{e^\varepsilon}{J} n_0^s \tag{11}$$

where $\varepsilon$ is the compaction strain of the solid constituent. We also further elaborate on the total mass balance of our binary mixture to obtain the combined mass balance relation

$$\nabla\cdot\boldsymbol{v}^s - n^s\dot{\varepsilon} = -\nabla\cdot\boldsymbol{v}^d. \tag{12}$$

Considering the localized format of the momentum balance in the spatial format, we obtain the balance relation for quasi-static behavior of the mixture, corresponding to the total form of the momentum balance specified in [29] as

$$\bar{\boldsymbol{\sigma}}\cdot\nabla + \hat{\rho}\boldsymbol{g} = \boldsymbol{0} \quad \forall x \in B \tag{13}$$

where $\bar{\boldsymbol{\sigma}} = \bar{\boldsymbol{\sigma}}^s + \boldsymbol{\sigma}^f$ is the total Cauchy stress, $\hat{\rho}$ is the bulk density, $\boldsymbol{g}$ is the gravity and $B$ represents the current configuration domain. In turn, $\bar{\boldsymbol{\sigma}}$ is related to the effective (constitutive) stress $\boldsymbol{\sigma}$ and the fluid pressure $p$ via the Terzaghi effective stress principle,

$$\bar{\boldsymbol{\sigma}} = \boldsymbol{\sigma} - p\mathbf{1} \tag{14}$$

In order to arrive at proper FE-formulation, we derive the weak form of the coupled set of Eqs. (12) and (13) and identify the primary variables as the placement $\boldsymbol{x} = \varphi^s(\boldsymbol{X}) \Rightarrow \boldsymbol{v}^s = \dot{\varphi}^s$ of solid particles and fluid pressure $p(\boldsymbol{x})$. Throughout the FE analyses, a Taylor–Hood element is adopted corresponding to quadratic interpolation for the placement and linear interpolation of the fluid pressure. For details description of the FE formulation cf. Larsson et al. [29].

### 3.2. Balance of energy and entropy inequality for isothermal behavior

Similar to the combined mass balance relationship, a combined balance of energy yields the change of internal energy of the mixture material. Likewise, the entropy inequality for the mixture material is obtained pertinent to isothermal behavior which combined with the energy equation (see [29] for details) yields

$$D = \underbrace{\boldsymbol{\sigma} : \boldsymbol{l} - n^s p\dot{\varepsilon} + \hat{\rho}^s\dot{\psi}^s}_{D^s} + \underbrace{\boldsymbol{v}^d\cdot\underbrace{(\rho^f\boldsymbol{g} - \nabla\cdot p)}_{\boldsymbol{h}_e^f}}_{D^i} \geqslant 0, \tag{15}$$

where $\psi^s$ is the free energy for the solid phase, $\boldsymbol{l}$ is the solid velocity gradient and $p$ is the intrinsic fluid pressure. The total mechanical dissipation $D$ is thus interpreted in terms of a few independent phenomenological mechanisms where $D^s \geqslant 0$ is the dissipation produced by the (homogenized) solid phase material considered as an independent process of the mixture. The contribution $D^i \geqslant 0$ represents dissipation induced by "drag"-interaction between the phases, where $\boldsymbol{h}_e^f$ is the effective drag force.

## 4. Constitutive relations

### 4.1. Response of the compressible fluid-filled fiber network

Given by the dissipation inequalities in (15), the proper stress response of the compressible (partly) fluid-filled fiber network may now be formulated. To this end, we formulate the dissipation produced by the solid phase for the entire component as

$$\langle D^s\rangle = \int_B D^s dv = \int_{B_0} JD^s dV \geqslant 0 \tag{16}$$

where the last expression was obtained after pull-back to the reference configuration $B_0$, as $dV$ is the infinitesimal volume element in $B_0$ while $dv$ is in the current configuration $B$. It may be noted that the integrand $JD^s$ in Eq. (16) may be rewritten in terms of the Kirchhoff stress $\boldsymbol{\tau} = J\boldsymbol{\sigma}$, the second Piola–Kirchhoff stress $\boldsymbol{S}$, the right Cauchy–Green deformation tensor $\boldsymbol{C}$ and the intrinsic fluid pressure $p$ as

$$JD^s = \boldsymbol{\tau} : \boldsymbol{l} - n^s p\dot{\varepsilon} - Jn^s\rho^s\dot{\psi}^s = \frac{1}{2}\boldsymbol{S} : \dot{\boldsymbol{C}} - Jn^s p\dot{\varepsilon} - \hat{\rho}_0^s\dot{\psi}^s, \tag{17}$$

where the last equality was obtained from mass conservation due to the stationarity of $M^s = M_0^s = \hat{\rho}_0^s$. Upon assuming, for simplicity, hyper-elasticity of the effective stress response we obtain the dependence $\psi^s(\boldsymbol{C}, \varepsilon, \varepsilon^p)$ in the free energy for the solid phase. In view of Eq. (17), the reduced dissipation obtained as

$$\dot{\psi}^s(\boldsymbol{C},\varepsilon,\varepsilon^p) = \psi^s_{mac}(\boldsymbol{C}) + \psi^s_{mes}(\varepsilon,\varepsilon^p) = \frac{\partial\psi^s_{mac}}{\partial\boldsymbol{C}} : \dot{\boldsymbol{C}} + \frac{\partial\psi^s_{mes}}{\partial\varepsilon}\dot{\varepsilon} + \frac{\partial\psi^s_{mes}}{\partial\varepsilon^p}\dot{\varepsilon}^p, \tag{18}$$

where we assumed an additive split of the free energy into macroscopic and mesoscopic parts. In view of (17), the final conclusion in (18) corresponds to the state equations

$$\boldsymbol{S} = 2\hat{\rho}_0^s\frac{\partial\psi^s_{mac}}{\partial\boldsymbol{C}}, \tag{19}$$

$$p = -\rho^s\frac{\partial\psi^s_{mes}}{\partial\varepsilon}, \tag{20}$$

where $\boldsymbol{S} = \bar{\boldsymbol{S}} - J\boldsymbol{C}^{-1}p$ is the effective second Piola–Kirchhoff stress due to the Terzaghi effective stress principle. In the following we subdivide the stress response in terms of the effective fiber bed response and the solid phase compaction associated with micro-infiltration induced by fluid pressure.

### 4.2. Effective fiber bed response

The effective response of the fiber bed is considered hyper-elastic governed by the stored energy function for Neo-Hooke like elastic material using isochoric–volumetric split written as

$$\psi^s_{mac}(\widehat{\boldsymbol{C}},J) = \psi^{s,iso}_{mac}(\widehat{\boldsymbol{C}}) + \psi^{s,vol}_{mac}(J) = G(\mathbf{1} : \widehat{\boldsymbol{C}} - 3) + J\frac{k^s E}{\beta - 1}\left(\frac{\phi_0^p}{J}\right)^\beta, \tag{21}$$

where $\widehat{\boldsymbol{C}} = J^{-2/3}\boldsymbol{F}^t \cdot \boldsymbol{F}$ and $\boldsymbol{F} = \partial\boldsymbol{x}/\partial\boldsymbol{X}$ is the deformation gradient. The parameters involved in this expression are the packing exponent $\beta$, taken as $\beta = 14.5$, and the $k^sE$ factor as $k^sE = 150 \times 10^2$ Pa [30]. We remark that, by having Eq. (21), the elastic small shear deformation properties of the fiber-bed (represented by the elastic shear modulus $G$) are generalized into the finite deformation regime. As to the response due to volumetric deformation, it was assumed that this response can be represented by the same packing law as was used for the fiber plies. In this case the argument of packing is the fiber volume fraction $\phi^p = \phi_0^p/J$ where $\phi_0^p$ is the initial volume fraction of particles. We remark that the assumption of isotropy of the fiber bed response means that the fiber plies possess no preferred orientation and may be justified within certain isotropy planes of loading of the fiber bed, which is the case in the verification example of Section 5.

### 4.3. Solid compaction and micro-infiltration

It was concluded that the solid phase compaction consists of an irreversible wetting process corresponding to the exclusion of voids in the micro-constituents and reversible component, basically due to elastic packing also induced by fluid pressure as shown in Fig. 2. As to elastic fiber packing, we note that uniaxial compression tests of fiber beds have been studied quite extensively in the literature, e.g. Kim et al. [31]. In the present paper, the semi-empirical elastic fiber packing law proposed in Toll [28] is directly generalized to the compressive response of the non-saturated region of a fiber bed consisting of voids and dry particles as

$$p + p_0 = kE\phi^\alpha, \tag{22}$$

where $p$ is the excess fluid pressure, relative to $p_0$, acting on a representative fiber ply, as shown in Fig. 2. Moreover $p_0 = kE\phi_0^\alpha$ is the configurational fluid pressure in the initially non-saturated representative fiber ply. The stored energy function associated with the elastic packing variable $\phi = \phi^{pd}/\phi^d$ is obtained for an increase of $\phi_0$ to $\phi$ (with due consideration to that the volume $V^{pd}$ is stationary during the elastic packing) as

$$W = \int_{\phi_0}^{\phi} kE(\phi^\alpha - \phi_0^\alpha)\frac{d\phi}{\phi} = \frac{kE}{\alpha}\left(\phi^\alpha - \phi_0^\alpha\left(1 + \alpha\log\left(\frac{\phi}{\phi_0^\alpha}\right)\right)\right). \tag{23}$$

The homogenized free energy is obtained from the energy equivalence $n^s\rho^s\psi^s = (\phi^{pd} + \phi^v)$ of the representative volume leading to

$$\begin{aligned}\psi^s_{mes} &= \frac{p_0}{\alpha}\left(\frac{1}{\rho^s} - \xi\frac{1}{\rho_0^s}\phi_0\right)\left(\gamma^\alpha - \alpha\log\left(\frac{\phi}{\phi_0^\alpha}\right) - 1\right)\\ &= \frac{1}{\rho_0^s}\frac{p_0}{\alpha}\frac{e^\varepsilon - \phi_0}{1 - \gamma\phi_0}\left(\gamma^\alpha - 1 - \alpha\log\left(\frac{\phi}{\phi_0^\alpha}\right)\right),\end{aligned} \tag{24}$$

where the first equality is specified in material arguments $\psi^s(\phi, \xi)$, whereas in the last equality a change in arguments has been made using the continuum compaction strain $\varepsilon$ and the elastic wetting strain $\varepsilon^p$, which is at hand for the numerical implementation. Moreover, we also introduced the ratio $\gamma = \phi/\phi_0$ formulated in arguments $\gamma(\varepsilon, \varepsilon^p)$as

$$\gamma = \frac{e^{\varepsilon^p} - \phi_0}{e^\varepsilon(1 - \phi_0) - \phi_0(1 - e^{\varepsilon^p})}. \tag{25}$$

Straightforward application of Eq. (20) yields the fluid pressures $p$ (relative to the configurational pressure $p_0$) as

$$p = p_0(\gamma^\alpha - 1). \tag{26}$$

In view of Eq. (22) we obtain in compliance form, the compaction as a function of the wetting and the fluid pressure read as

$$e^\varepsilon = \frac{\left(\frac{p_0 + p}{p_0}\right)^{-1/\alpha}(e^{\varepsilon^p} - \phi_0) + (1 - e^{\varepsilon^p})\phi_0}{1 - \phi_0}. \tag{27}$$

Now, considering the rate form of relation (27) we formally obtain

$$e^\varepsilon\dot{\varepsilon} = \underbrace{-\frac{e^{\varepsilon^p} - \phi_0}{\alpha(p + p_0)(1 - \phi_0)}\left(\frac{p + p_0}{p_0}\right)^{-1/\alpha}\dot{p}}_{f(p,\varepsilon^p)\dot{p}} - \underbrace{e^{\varepsilon^p}\frac{\left(\left(\frac{p+p_0}{p_0}\right)^{-1/\alpha} - \phi_0\right)}{1 - \phi_0}\frac{p}{\mu}}_{g(p,\varepsilon^p)p}, \tag{28}$$

where it was used that the wetting is a diffusive process represented by the viscous evolution

$$\dot{\varepsilon}^p = -\frac{p}{\mu}. \tag{29}$$

The parameter $\mu$ represents the viscous resistance for penetration of liquid into the bulk fibers, which is defined as

$$\mu = \frac{v(1 - \phi_0)\zeta^2}{K_{mes}}, \tag{30}$$

where $v$ is the fluid viscosity and $\zeta$ is the wetting length. The mesoscopic permeability $K_{mes}$ for fiber plies, which is the permeability through the fiber bed, is calculated based on the Gebart equation [32] for hexagonal fiber packing as

$$K_{mes} = \frac{16r^2}{9\pi\sqrt{2}}\left[\sqrt{\frac{\pi}{2\phi_0\sqrt{3}}} - 1\right]^{5/2}. \tag{31}$$

where $r$ is the fiber radius. For later use, we introduced $e^\varepsilon\dot{\varepsilon}$ in compact form in Eq. (28) using the functions $f(p, \varepsilon^p)$ and $g(p, \varepsilon^p)$ as $e^\varepsilon\dot{\varepsilon} = f\dot{p} + gp$. It is noted that the function $g$ represents the viscous resistance against wetting, whereas the function $f$ represents instantaneous elastic packing increment for a pressure increase.

### 4.4. Anisotropic Darcian solid–fluid interactions

The last contribution $D^i \geqslant 0$ of (15) represents dissipation induced by "drag"-interaction between the phases. To accommodate this dissipation, the effective drag force $\boldsymbol{h}_e^f$ (or hydraulic gradient with negative sign) is chosen to ensure positive dissipation via Darcy's law

$$\boldsymbol{v}^d = -\frac{1}{v}\boldsymbol{K}_{mac}\cdot\boldsymbol{h}_e^f, \qquad \boldsymbol{h}_e^f = \nabla p, \tag{32}$$

where $\boldsymbol{K}_{mac}$ is the anisotropic permeability tensor. In order to derive the permeability for the considered VBO prepreg, a special model was developed by Rouhi et al. [33] to account for (i) the macroscopic flow between the layers and (ii) the infiltration flow into the dry (mesoscopic) fiber plies as

$$\begin{aligned}\boldsymbol{v}^d &= -\frac{1}{v}((K_{mes}(1 - \phi^l) + K_{Ch}\phi^l)(\boldsymbol{1} - \boldsymbol{M}) + K_{mes}\boldsymbol{M})\cdot\boldsymbol{h}_e^f\\ &= \frac{1}{v}\boldsymbol{K}_{mac}\cdot\boldsymbol{h}_e^f,\end{aligned} \tag{33}$$

where $K_{mes}$ is the permeability through the fiber, $K_{Ch}$ is the permeability through the channel, $\phi^l$ is liquid volume fraction and $\boldsymbol{M} = \boldsymbol{T}\otimes\boldsymbol{T}$ is the structure tensor related to the director field $\boldsymbol{T}$, cf. Fig. 3. The permeability through the channel may be approximated considering the resistance to viscous flow within a rectangular channel, cf. Fig. 4 [33]

$$K_{Ch} = \frac{(H_0\lambda_{||} - h_0^s)^2}{12}. \tag{34}$$

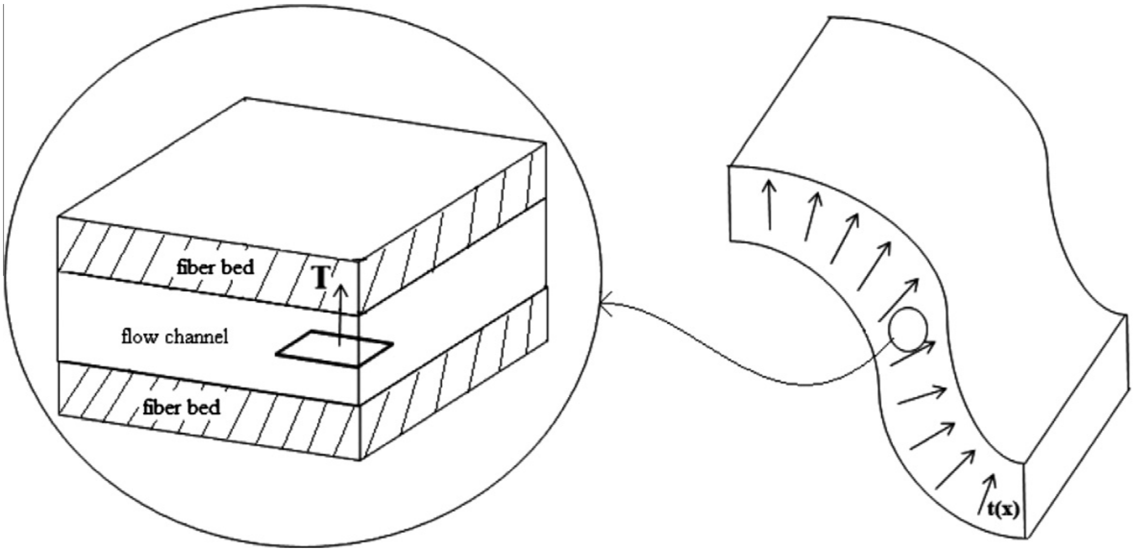

**Fig. 3.** Flow channel with orientation ***T*** and fiber bed stacks.

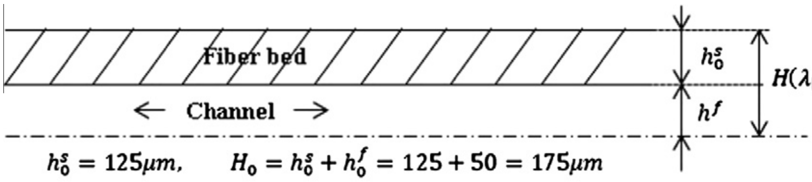

**Fig. 4.** Distance between fiber layers and flow channel.

where $\lambda_{||}$ is the continuum stretch in the direction of $\boldsymbol{T}$, $H_0$ is the half thickness of the initial prepreg, $h_0^s$ is the initial thickness of fiber bed and $h_0^f$ is the half of the initial thickness of the channel between the plies.

## 5. A representative relaxation test of a fluid-filled preform

In order to numerically test the framework we consider a compressive relaxation test applied to a fluid filled fiber network, which is related to press forming of VBO prepregs. Considering the press forming simulation, we will have the possibility of having an experimental verification of the modeled generic algorithm, which is an undergoing work. Generally speaking, out-of-autoclave processes are usually done while vacuum pressure is the main load over prepregs, but in a press forming process we apply an elevated load which affects the process time from being a matter of minutes to seconds.

The model in Eq. (21) is used to represent the effective stress response of the fiber bed. In addition, the permeability model discussed in Eq. (34) was used to model the macroscopic Darcian permeability. The involved material parameters represent a system of fiber plies of carbon fiber and epoxy resin. To this end, parameters are sourced from [30] where for the permeability $K_{Ch}$, the distance between fiber layers was $h = 20 \times 10^{-6}$, and the initial particle volume fraction was $\phi_0^p = 0.48$. As to the mechanical fiber bed response, the shear modulus was taken from [30] as $G = 50 \times 10^6$ Pa, the $k^sE$ factor in Eq. (21) was $k^sE = 150 \times 10^2$ Pa, and the packing exponent of the fiber bed is $\beta = 0.45$. Moreover, for the micro-infiltration, the liquid viscosity was chosen as $\nu = 100$ Pa s, the initial unsaturated porosity $n_0 = 0.85$ and the initial local fiber content volume fraction $\phi_0 = 0.55$. The wetting length was $\zeta = 50 \times 10^{-6}$ m, the fiber radius is $r = 3.5 \times 10^{-6}$ m, the $kE$ factor as in Eq. (23) is $kE = 500 \times 10^6$ Pa, and the exponent of the microscopic packing exponent is $\alpha = 14.5$.

The analyzed planar specimen is shown in Fig. 5 along with the applied loading consisting of a prescribed vertical displacement $r$ on the top boundary and fixed displacements on the lower boundary of the plate. As to the fluid pressure boundary conditions two

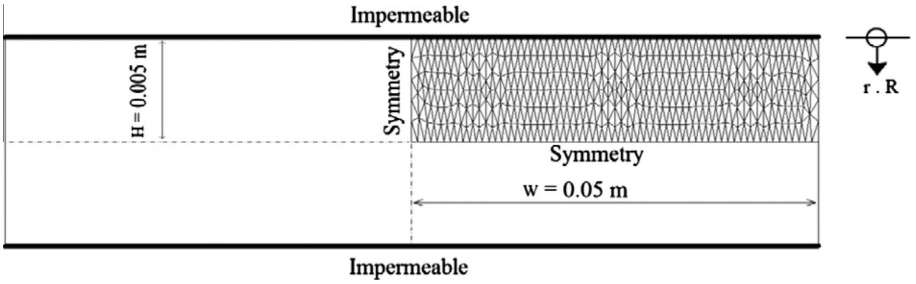

**Fig. 5.** Analyzed rectangular specimen with initial geometry and boundary conditions. Two cases are considered: (1) $p = 0$ along the vertical boundaries defining the partly drained condition and (2) the vertical boundaries are impermeable defining the globally un-drained condition (corresponding to $p = unknown$ along the vertical boundaries).

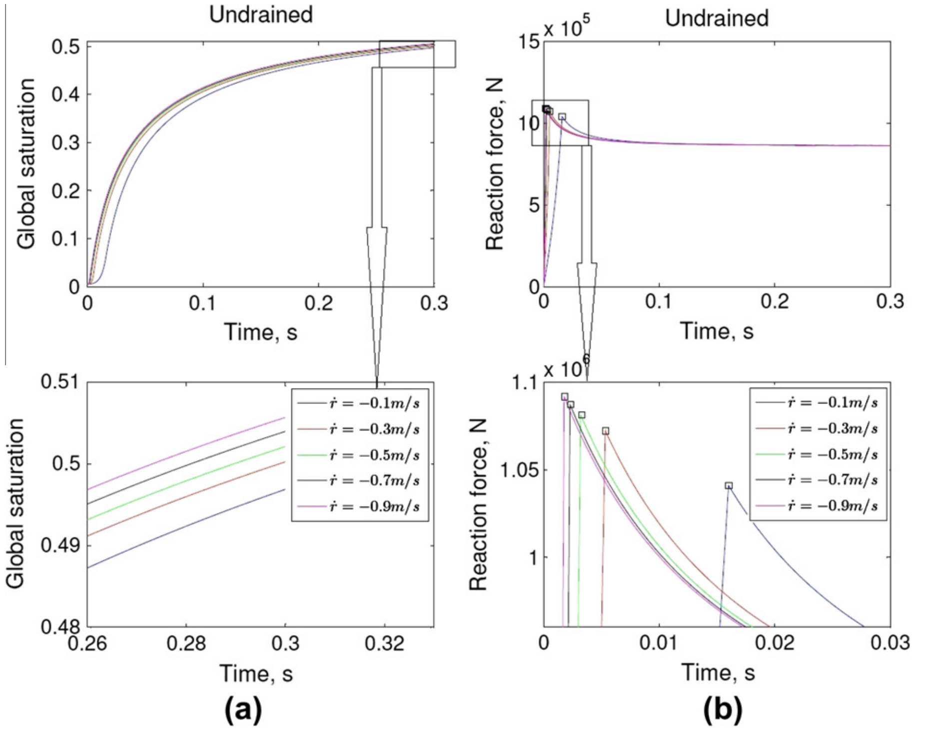

**Fig. 6.** Relaxation test at globally un-drained condition with respect to different initial loading rates. (a) Resulting global saturation degrees versus process time and (b) resulting reaction forces versus time. (For interpretation of the references to color in this figure legend, the reader is referred to the web version of this article.)

different types are considered. The first case corresponds to macroscopically *un-drained conditions*, where all outer boundaries are considered impermeable. The second case is the *partly drained condition*, corresponding to drainage along the vertical boundaries of the specimen, where the fluid pressure is prescribed to zero. The prescribed displacement is thus considered as a controlled displacement $r$ on the top boundary, which is ramped (based on a chosen time step) for different loading rates $\dot{r}$ up to the total compression $r/H = 0.2$, where $H$ is the height of the specimen. Relaxation is thereafter considered by setting $\dot{r} = 0$ after the specimen

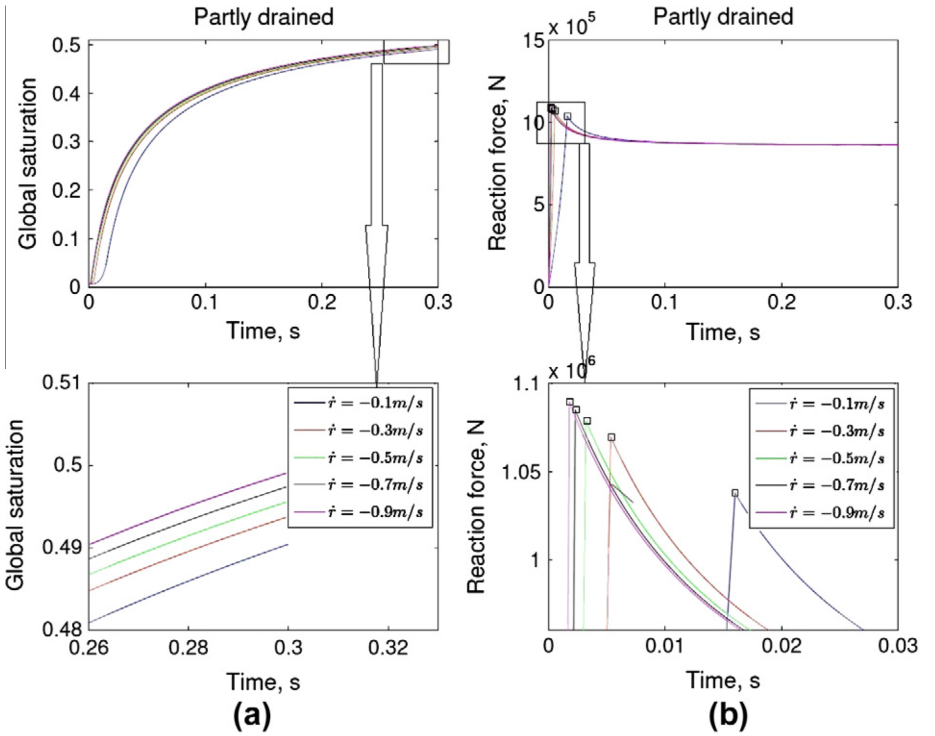

**Fig. 7.** Relaxation test at partially drained conditions with respect to different initial loading rates. (a) Resulting global saturation degrees versus process time and (b) resulting reaction forces versus time. (For interpretation of the references to color in this figure legend, the reader is referred to the web version of this article.)

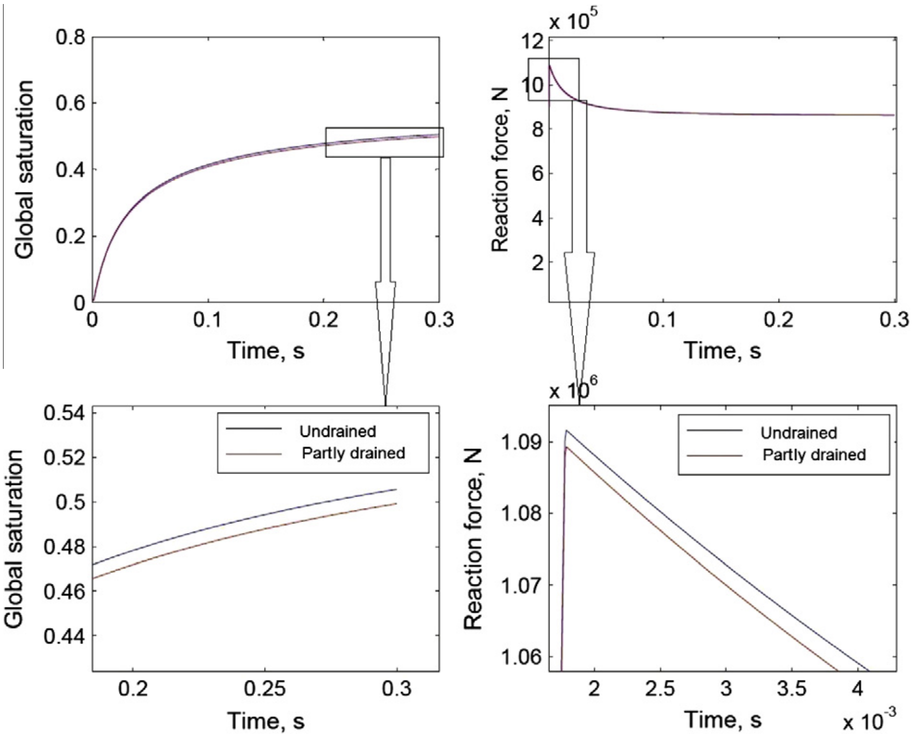

**Fig. 8.** Comparison between relaxation tests for globally un-drained and partially drained conditions at the initial loading rate $\dot{r} = -0.5$ m/s. (a) Global saturation degree versus time and (b) reaction forces versus time. (For interpretation of the references to color in this figure legend, the reader is referred to the web version of this article.)

has been compressed 20%. On the basis of this loading program, we assess the wet out in the specimen depending on the rate of initial loading $\dot{r}$ and relaxation time. For this purpose we consider five different rates chosen as, $\dot{r} = 0.1$ m/s, $\dot{r} = 0.3$ m/s, $\dot{r} = 0.5$ m/s, $\dot{r} = 0.7$ m/s, $\dot{r} = 0.9$ m/s.

As shown in Fig. 5, due to the symmetry in the plate and the boundary conditions, only one quarter of the plate is analyzed. The results from the initial loading-relaxation test are discussed in terms of the temporal evolution of the global saturation degree measure $\xi$, defined as the volume average of the saturation degrees within all elements of the mesh. Relaxation of the specimen is considered as the temporal variation of the reaction force $R$ due to the applied loading.

Fig. 6 shows the reaction force and the global saturation degree versus time for the globally un-drained case. We observe from Fig. 6 that, as the initial compression rate increases, the saturation rate and the reaction forces are increased. However, after relaxation, they approach more or less the same value for all rates. It may be observed that the highest reaction force, $R = 1.091$ MN, equivalent to 21.82 MPa average stress on the specimen, was obtained when we have the highest rate, $\dot{r} = -0.9$ m/s as compared to $R = 1.04$ MN, equivalent to 21 MPa average stress, for the lowest rate $\dot{r} = -0.1$ m/s.

The reaction forces increases by increasing the displacement rates because higher rates results in higher pressure gradient and consequently higher Darcian velocity while keeping the isotropic permeability constant. The similar rate effects are also observed on the level of saturation degree. We thus conclude that a higher level of saturation (and reaction forces) may thus be achieved upon increasing the initial (prescribed) displacement rate.

The result from the partly drained case is shown in Fig. 7. For the considered parameters and loading cases, the resulting behavior is very much the same and very close to the result from the un-drained case shown in Fig. 6 when considering the overall saturation degree level, the reaction force and the process time. The difference between the globally un-drained and partly drained cases, in terms of saturation degree and reaction forces, is shown in Fig. 8. One can observe from Fig. 8 that in the drained case we obtain a slightly lower saturation degree level, $\xi = 0.4992$ versus $\xi = 0.5057$ for the un-drained case. We also observe a lower reaction forces for the partly drained case, $R = 1.089$ MN ($\sigma = 21.78$ MPa) versus $R = 1.091$ MN ($\sigma = 21.82$ MPa) for the un-drained case. The difference between the two cases is not noticeable since we are comparing the average global saturation degree and reaction forces. Moreover, a comparison between the two cases is also displayed for the local saturation degree in Fig. 9 where it is noted that the effect of the different pressure descriptions along the side boundary significantly affects the level and distribution of the local saturation degree. The drained case generally reduces the magnitudes of the fluid pressure on the boundary as

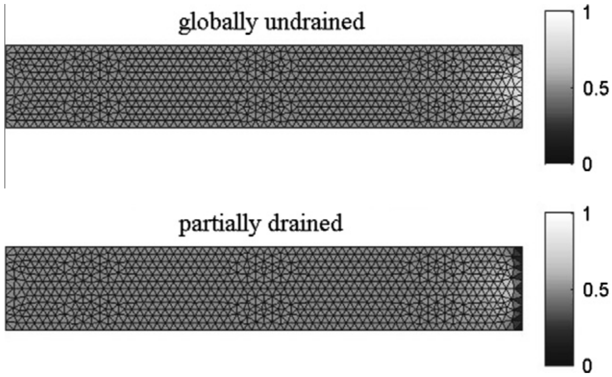

**Fig. 9.** Comparison between local saturation degree distributions obtained in relaxation tests for globally un-drained and partially drained conditions at the initial loading rate $\dot{r} = -0.5$ m/s.

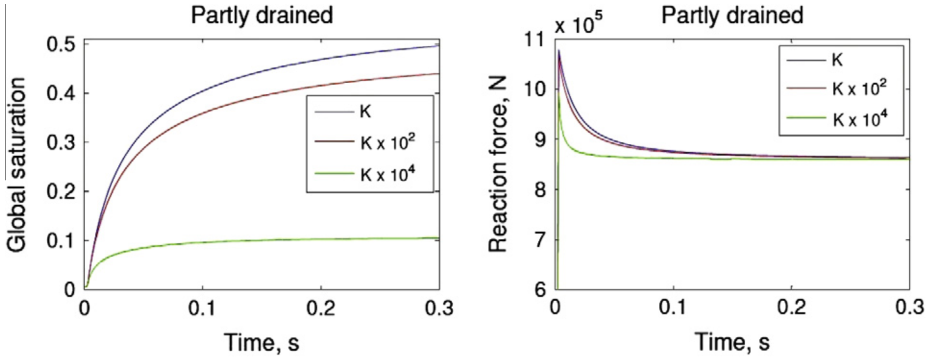

**Fig. 10.** Global saturation and reaction forces for different value of macroscopic permeability, $K_{mac}$ at $\dot{r} = -0.5$ m/s. (For interpretation of the references to color in this figure legend, the reader is referred to the web version of this article.)

compared to un-drained case, leading to slower evolution of the micro-infiltration for the drained case.

From Figs. 6 and 7, one can observe that the time needed to reach the desired compaction before unloading is much smaller than the total time required to reach the relaxation stage; the initial loading step time is around 0.01 s while the total simulation time to reach to a stable level is around 0.1 s. The numerical setup is also sensitive to the time stepping. The displacement rate and the time steps are related so that a higher rate of deformation requires a smaller time step for a stable solution of the nonlinear set of equations. If we decrease the rate, we can increase the time step intervals. For a stable solution at the chosen displacement rates the process is simulated for 30,000 time steps with time interval being 0.00001; the total process (real) time is 0.3 s.

It is also of interest to consider the effect of Darcy flow and macroscopic permeability, $K_{mac}$ on the level of saturation and reaction forces in *drained* case. This is since in the case of Darcian velocity, $\boldsymbol{v}^d$ is the key to drainage as the flow on the boundaries is driven by Darcian velocity.

To do so, three different values of $K_{mac}$ were considered. As shown in Fig. 10 increasing the permeability results is decrease of the level of saturation. Even the reaction forces decreases, especially in the extreme case.

## 6. Concluding remarks

In the present paper we proposed a framework for the modeling of a family of Out-Of-Autoclave (OOA) manufacturing processes of fiber reinforced composites such as Vacuum Bag Only (VBO) and Engineering Vacuum Channel (EVaC). However, our generic framework is towards holistic modeling of (in principle) all possible composites manufacturing processes. Therefore, the present continuum model is a specialization of a more general two-phase continuum formulation for composites processing problems, including infiltration, consolidation and forming. A special porous media formulation has been developed aimed for a dual-scale coupled flow–deformation process. In this framework, constitutive relations concerning four different mechanisms governing the process of press forming have been described involving (i) constitutive effective stress response of the fiber bed, (ii) infiltration of resin into fiber plies, (iii) elastic packing response of the plies, and (iv) Darcy's law governing the macroscopic interaction between the two phases. As such it is thermodynamically consistent and satisfies the balances of energy, mass and momentum. Due to the micro-mechanical basis, all parameters involved in the model have a clear physical meaning and are measurable, in principle.

The computational FE-treatment of the proposed model in conjunction with nonlinear kinematics is numerically implemented. In the numerical example, we have considered a planar fluid saturated fiber bed network subjected to relaxation tests representing press forming operation. The tests were simulated and the principal behavior for the different cases of globally un-drained and partly drained conditions was established. The dependence on the rate of ramp-up loading in the relaxation test of the planar fluid filled network was determined. A comparison between the local saturation degree distributions during the relaxation test for these cases was also made. The effect of macroscopic permeability for the partly drained condition was investigated with respect to the relaxation test.

The difference between the real out-of-autoclave or VBO prepreg with the simulated press forming process here is that loads higher than vacuum pressure are applied during the process which makes the manufacturing time faster. By doing so, an experimental verification for the simulation, which is missing in this paper, become possible by a series of press forming experiments which is an undergoing research work.

## References

[1] Kratz James. Processing composite sandwich structures using out-of-autoclave technology. Master thesis, McGill University, August 2009.
[2] Thomas S, Nutt SR. In situ estimation of through-thickness resin flow using ultrasound. Compos Sci Technol 2008;68:3093–8.
[3] Grunenfelder LK, Nutt SR. Void formation in composite prepregs – effect of dissolved moisture. Compos Sci Technol 2010;70:2304–9.
[4] Hubert P, Poursartip A. Review of flow and compaction modeling relevant to thermoset matrix laminate processing. J Reinf Plast Compos 1998;17(4):286–318.
[5] Ngo N et al. Recent developments encompassing non-isothermal/isothermal liquid composite molding process modeling/analysis: physically accurate, computationally effective, and affordable simulations and validations. J Thermoplast Compos Mater 1998;11(6):493–532.
[6] Trochu F, Gauvin R, Gao D-M. Numerical analysis of the resin transfer molding process by the finite element method. Adv Polym Technol 1993;12(4):329–42.
[7] Lee LJ, Young WB, Lin RJ. Mold filling and cure modeling of RTM and SRIM processes. Compos Struct 1994;27(1–2):109–20.
[8] Luo J et al. Optimum tooling design for resin transfer molding with virtual manufacturing and artificial intelligence. Compos A – Appl Sci Manuf 2001;32(6):877–88.
[9] Bechet E et al. Adaptive mesh generation for mould filling problems in resin transfer moulding. Compos A – Appl Sci Manuf 2003;34(9):813–34.
[10] Simacek P, Advani SG. Desirable features in mold filling simulations for liquid molding processes. Polym Compos 2004;25:355–67.
[11] Parnas RS, Phelan FR. The effect of heterogeneous porous media on mold filling in resin transfer molding. Sample Quart 1991;22:53–60.
[12] Pillai KM, Advani SG. A model for unsaturated flow in woven fiber preforms during mold filling in resin transfer molding. J Compos Mater 1998;32(19):1753–83.
[13] Binetruy C, Hilaire B, Pabiot J. The interactions between flows occurring inside and outside fabric tows during RTM. Compos Sci Technol 1997;57(5):587.
[14] Lekakou C, Bader MG. Mathematical modelling of macro- and micro-infiltration in resin transfer moulding (RTM. Compos A – Appl Sci Manuf 1998;29(1–2):29.
[15] Binetruy C, Hilaire B. Tow impregnation model and void formation mechanisms during RTM. J Compos Mater 1998;32(3):223–45.

[16] Ngo ND, Tamma KK. Microscale permeability predictions of porous fibrous media. Int J Heat Mass Transf 2001;44(16):3135.

[17] Pillai KM. Modeling the unsaturated flow in liquid composite molding processes: a review and some thoughts. Compos A – Appl Sci Manuf 2002;33(7):1007.

[18] Takano N et al. Microstructure-based evaluation of the influence of woven architecture on permeability by asymptotic homogenization theory. Compos Sci Technol 2002;62(10–11):1347.

[19] Grujicic M, Chittajallu KM, Walsh S. Effect of shear, compaction and nesting on permeability of the orthogonal plain-weave fabric preforms. Mater Chem Phys 2004;86(2–3):358.

[20] Simacek P, Advani SG. A numerical model to predict fiber tow saturation during liquid composite molding. Compos Sci Technol 2003;63(12):1725.

[21] Correia NC, Robitaille F, Long AC, Rudd CD, Simacek P, Advani SG. Analysis of the vacuum infusion moulding process: I. Analytical formulation. Compos A – Appl Sci Manuf 2005;36(12):1645–56.

[22] Zhou F, Kuentzer N, Simacek P, Advani SG, Walsh S. Analytic characterization of the permeability of dual-scale fibrous porous media. Compos Sci Technol 2006;66(15):2795–803.

[23] Schell JSU, Deleglise M, Binetruy C, Krawczak P, Ermanni P. Numerical prediction and experimental characterisation of meso-scale-voids in liquid composite moulding. Compos A – Appl Sci Manuf 2007;38(12):2460–70.

[24] Larsson J, Larsson R. Non-linear analysis of nearly saturated porous media – theoretical and numerical formulation. Comput Methods Appl Mech Eng 2002;191:3885–907.

[25] Centea T, Hubert P. Measuring the impregnation of an out-of-autoclave prepreg by micro-CT. Compos Sci Technol 2011;71:593–9.

[26] Slade J, Pillai KM, Advani SG. Investigation of unsaturated flow in woven, braided and stitched fiber mats during mold-filling in resin transfer molding. Polym Compos 2001;22(4):491–505.

[27] Larsson R, Wysocki M, Toll S. Process-modelling of composites using two-phase porous media theory. Eur J Mech A/Solids 2004;23:15–36.

[28] Toll S. Packing mechanics of fiber reinforcements. Polym Eng Sci 1998;38(8):1337–50.

[29] Larsson R, Rouhi M, Wysocki M. Free surface flow and preform deformation in composites manufacturing based on porous media theory. Eur J Mech A/Solids 2012;31:1–12.

[30] Wysocki Maciej, Larsson Ragnar, Toll Staffan. Modelling the consolidation of partially impregnated prepregs. In: Proceedings of 17th international conference on composite materials, Edinburgh, UK.

[31] Kim YR, McCarthy SP, Fanucci JP. Compressibility and relaxation of fiber reinforcements during composite processing. Polym Compos 1991;12(1):13–9.

[32] Gebart BR. Permeability of unidirectional reinforcements for RTM. J Compos Mater 1992;26:1100. http://dx.doi.org/10.1177/002199839202600802.

[33] Rouhi M, Wysocki M, Larsson R. Modeling the constitutive response of an anisotropic dual-scale flow. In: Proceeding of 11th international conference ‘flow processes on manufacturing of composite manufacturing (FPCM-11)’, Auckland, New Zealand; 2012.